COUPLED CFD ANALYSIS OF THE HOT GAS AND THE COOLANT FLOW IN EFFUSION COOLED COMBUSTION CHAMBERS

J. Riccius, D. Greuel, O. Haidn
DLR Lampoldshausen
74239 Hardthausen
Germany

T. Leicht
Dresden University of Technology
Germany

1. MOTIVATION

All over the world, rocket engine design engineers are faced with an ever increasing demand for higher performance and reliability as well as reduced cost. In order to improve the efficiency of current state-of-the-art core engines, operating at combustion chamber pressures above 10 MPa, a hot gas pressure of up to 25 MPa is desirable. In consequence of the proportional increase of the heat transfer from the hot gas to the chamber wall at such high pressure levels, alternative cooling methods to the conventional regenerative cooling are proposed to ensure the thermal protection of the chamber liner. Effusion cooling of a porous combustion chamber wall made of carbon fiber reinforced carbon (C/C) seems to be one of the most prospective techniques to fulfill this requirement. Due to the high temperature resistance of this material, the demand of coolant fluid to protect the liner and therefore the pressure drop in the coolant supply system is minimized. A constant improvement of the material characteristics and an optimization of the design of the combustion chamber wall with respect to the coolant distribution should lead to an acceptable coolant demand for a practical application of this technology. Following this approach, numerical analyses have been performed with the objective of a better understanding of the coolant flow dynamics inside the porous wall and the coolant - hot gas interaction at the wall outlet.

2. GENERAL APPROACH

Since a few years DLR works on the field of effusion technology [1],[2]. In the current paper, underlying CFD analyses are shown. These CFD analyses are based of the following principles:

- rotatory symmetric 2d model
- solution of the Navier-Stokes equations
- coupled analysis of the hot gas and the coolant flow („multi species“)
- compressible solution algorithm, ideal gas equation
- $k-\varepsilon$ turbulence model in the combustion chamber, assumption of laminar flow in the porous chamber wall
- „distributed resistance“ according to Forchheimer in the chamber wall

3. CFD MODELS

3.1. Basic equations

3.1.1. Continuity equation

A coupled analysis of the hot gas and the coolant flow in the combustion chamber is performed. As a stationary rotatory symmetric behavior is assumed, the continuity equation reads as:

$$\frac{1}{r}\frac{\partial(r\rho v_r)}{\partial r}+\frac{\partial(\rho v_x)}{\partial x}=0 \quad (1)$$

with:

x, r: axial and radial direction of the polar co-ordinates, respectively

v_x, v_r: axial and radial components of the

v: velocity vector, respectively
ρ: density

3.1.2. Navier Stokes equations

The Navier Stokes equations in polar coordinates are given as:

$$v_r\frac{\partial(\rho v_r)}{\partial r}+v_x\frac{\partial(\rho v_r)}{\partial x} = -\frac{\partial p}{\partial r}+\frac{\mu}{\rho}\left[\frac{\partial}{\partial r}\left(\frac{1}{r}\frac{\partial}{\partial r}(r\rho v_r)\right)+\frac{\partial^2(\rho v_r)}{\partial x^2}\right] \quad (2)$$

$$v_r\frac{\partial(\rho v_x)}{\partial r}+v_x\frac{\partial(\rho v_x)}{\partial x} = -\frac{\partial p}{\partial x}+\frac{\mu}{\rho}\left[\frac{1}{r}\frac{\partial}{\partial r}\left(r\frac{\partial(\rho v_x)}{\partial r}\right)+\frac{\partial^2(\rho v_x)}{\partial x^2}\right] \quad (3)$$

with:

p: pressure
μ: dynamic viscosity

3.1.3. Species transport equation

Although the combustion of the fuel and the oxidizer is not modeled in detail, two species have to be considered: the product of the combustion (e.g. steam, if hydrogen and oxygen is burned) and the coolant (e.g. hydrogen). In polar co-ordinates, the transport equation for the i th species reads as:

$$\frac{1}{r}\frac{\partial(r\rho\Phi_i v_r)}{\partial r}+\frac{\partial(\rho\Phi_i v_x)}{\partial x} -\frac{\partial}{\partial r}\left(\rho D_{m_i}\frac{\partial\Phi_i}{\partial r}\right)-\frac{\partial}{\partial x}\left(\rho D_{m_i}\frac{\partial\Phi_i}{\partial x}\right)=0 \quad (4)$$

with:

$\Phi_i=\frac{m_i}{\sum_{j=1}^{n}m_j}$: mass fraction of the i th species in relation to the total mass of all species
n: number of considered species
D_{m_i}: mass diffusion coefficient of the i th species

3.1.4. Energy equation

Under the assumption of vanishing energy sources, the energy equation for stationary analyses is given as:

$$\frac{\partial}{\partial x}(\rho v_x C_p T_0)+\frac{1}{r}\frac{\partial}{\partial r}(r\rho v_r C_p T_0) = \frac{\partial}{\partial x}\left(\lambda\frac{\partial T_0}{\partial x}\right)+\frac{1}{r}\frac{\partial}{\partial r}\left(r\lambda\frac{\partial T_0}{\partial r}\right)+W_V+E^K+\phi \quad (5)$$

$$T_0=T+\frac{v^2}{2C_p} \quad (6)$$

$$W_V=v_j\mu\left(\frac{\partial}{\partial x_i}\frac{\partial v_j}{\partial x_i}+\frac{\partial}{\partial x_k}\frac{\partial v_k}{\partial x_j}\right) \quad (7)$$

$$E^K=-\frac{\partial}{\partial x}\left[\frac{\lambda}{C_p}\frac{\partial}{\partial x}\left(\frac{1}{2}|v^2|\right)\right] -\frac{\partial}{\partial r}\left[\frac{\lambda}{C_p}\frac{\partial}{\partial r}\left(\frac{1}{2}|v^2|\right)\right] \quad (8)$$

$$\phi=\mu\left(\frac{\partial v_i}{\partial x_k}+\frac{\partial v_k}{\partial x_i}\right)\frac{\partial v_i}{\partial x_k} \quad (9)$$

with:

C_p: specific heat
T_0: total temperature
λ: thermal conductivity
W_V: volume change work
E^K: kinetic energy
ϕ: dissipation energy
T: static temperature
$v=\sqrt{v_x^2+v_y^2}$: velocity

3.1.5. Ideal Gas equation

The Ideal Gas equation is applied, which in its nominal value formulation reads as:

$$\rho=\rho_n\frac{pT_n}{p_nT} \quad (10)$$

with:

T_n: nominal temperature
p_n: nominal pressure
ρ_n: density at nominal temperature and nominal pressure

3.2. Temperature dependent variation of the fluid properties

3.2.1. Sutherland variation of the viscosity

The temperature dependent variation of the viscosity is modeled by the following equation:

$$\mu = \mu_n \left(\frac{T}{T_{n,\mu}} \right)^{1,5} \frac{T_{n,\mu} + \varsigma_\mu}{T + \varsigma_\mu} \tag{11}$$

with:

$T_{n,\mu}$: nominal temperature for the specification of the viscosity
μ_n: viscosity at nominal temperature
ς_μ: coefficient for the temperature dependent definition of the viscosity according to Sutherland

3.2.2. Sutherland variation of the thermal conductivity

The temperature dependent variation of the thermal conductivity is modeled by (12):

$$\lambda = \lambda_n \left(\frac{T}{T_{n,\lambda}} \right)^{1,5} \frac{T_{n,\lambda} + \varsigma_\lambda}{T + \varsigma_\lambda} \tag{12}$$

with:

$T_{n,\lambda}$: nominal temperature for the specification of the thermal conductivity
λ_n: thermal conductivity at nominal temperature
ς_λ: coefficient for the Sutherland variation of the thermal conductivity

3.3. Model specification for the hot gas flow

In the hot gas part of the combustion chamber, the $k-\varepsilon$ turbulence model [3], [4] is applied. At wall boundaries, a logarithmic wall function is used [5].

3.4. Model specification for the coolant flow

In the combustion chamber wall area, no turbulence model is applied. In order to allow for a time efficient solution of the given problem, the porous wall material is not modeled in detail. However, the influence of the porous medium to the fluid flow in the combustion chamber wall is taken into account as a „distributed resistance“ based on the Forchheimer model.

$$\frac{\partial p}{\partial x} = -\left\{ K_x \rho v_x |v| + C_x \mu v_x \right\}, \qquad \frac{\partial p}{\partial r} = -\left\{ K_r \rho v_r |v| + C_r \mu v_r \right\} \tag{13}$$

with:

K_x, K_r: head loss parameters in axial and radial direction
C_x, C_x: permeability values in axial and radial direction
x, r: polar co-ordinates
v_x, v_r: radial and axial components of the Darcy velocity

The Darcy velocity v is the velocity of the fluid in case the porous medium is eliminated, but the total mass flow rate is maintained. The average velocity v_{pore} in the pores of a porous wall material is given as:

$$v_{pore} = \frac{1}{\varepsilon} v \tag{14}$$

$$\varepsilon = \frac{V_{pores}}{V_{total}} = \frac{V_{pores}}{V_{pores} + V_{solid}} \tag{15}$$

with:

v_{pore}: averaged velocity in the pores of the porous medium
v: Darcy velocity
ε: effective porosity
V_{pores}: volume of the pores (that means: volume of the hollow part) of the porous medium
V_{total}: total volume (pores and solid material) of the porous medium
V_{solid}: volume of the solid part of the porous medium

From equation (15) follows, that the porosity is always smaller than 1 and therefore, the Darcy velocity is smaller than the actual velocity in the pores.

4. DETERMINATION OF THE FLUID PROPERTIES

4.1. Determination of the Forchheimer parameters

The Forchheimer parameters K_x, K_r, C_x and C_x, which describe the distributed resistance, are determined by means of least square fit analyses of experimental results, given for a series of pressure differences for a test sample (exemplary given for the axial flow direction):

(16) $$\sum_{i=1}^{N}(\dot{m}_{num,i}(K_x,C_x)-\dot{m}_{\exp,i})^2 \xrightarrow{K_x,C_x} \min$$

with:

N: number of pressure difference values, which are taken into account for the least square fit analysis

$\dot{m}_{num,i}(K_x,C_x)$: numerically determined mass flow rate for i-th pressure difference (dependent on the head loss and permeability parameters)

$\dot{m}_{\exp,i}$: experimentally determined mass flow rate for i-th pressure difference

The good coincidence of experimental and numerical results with least square fitted parameters is shown in FIG 1. and FIG 2.

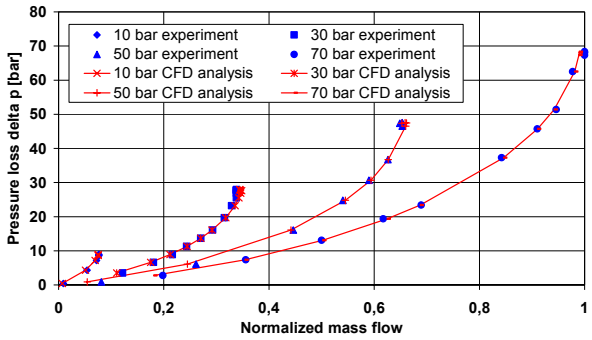

FIG 1. Comparison of experimental results and CFD results with least square fitted Forchheimer parameters for cylindrical test sample for axial fluid flow parameters, 293 Kelvin.

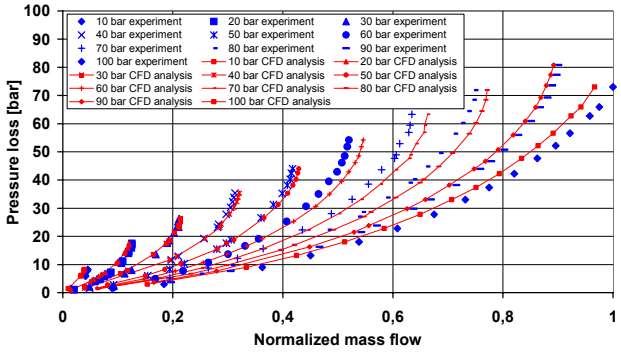

FIG 2. Comparison of experimental results and CFD results with least square fitted Forchheimer parameters for cylindrical test sample for radial fluid flow parameters, 293 Kelvin.

Based on the least square fitted Forchheimer parameters of the cylindrical test samples, a coupled CFD analysis of the hot gas flow in the combustion chamber and the coolant flow in the combustion chamber wall is performed.

4.2. Determination of the Sutherland parameters

For the determination of the Sutherland parameters ς_μ and ς_λ, a similar method as shown in section 4.1 was applied. The resulting variation of the thermal conductivity and the dynamic viscosity for hydrogen is shown in subsections 4.2.1 and 4.2.2.

4.2.1. Fitted Sutherland model for hydrogen

The least square fitted Sutherland variation of the thermal conductivity for hydrogen is given in FIG 3. The coincidence between the literature values and the fitted Sutherland model values in FIG 3. is rather poor. The distribution of the model error – too small thermal conductivity values for very low as well as very high temperature values and too large thermal conductivity values in the medium temperature range – indicates a successful least square fit of the literature data. This indicates that the poor coincidence with the literature data is due to limitations of the Sutherland model.

However – as shown in FIG 4. - a smaller Sutherland model error can be achieved for the approximation of the dynamic viscosity of hydrogen.

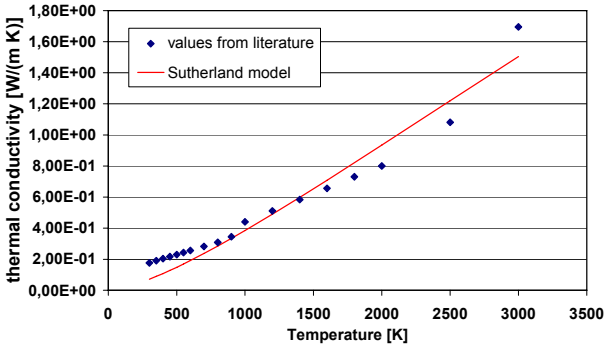

FIG 3. Temperature dependent thermal conductivity of hydrogen at a pressure level of 12 MPa.

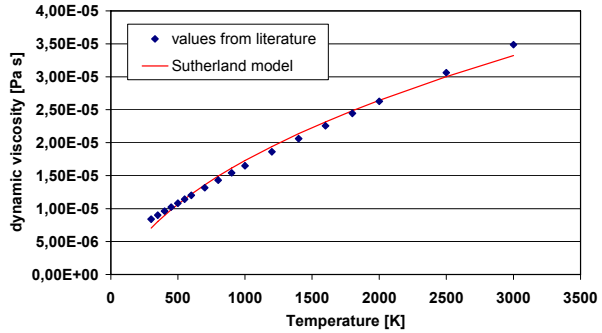

FIG 4. Temperature dependent dynamic viscosity of hydrogen at a pressure level of 12 MPa.

4.2.2. Fitted Sutherland model for steam

The Sutherland variation of the thermal conductivity and the dynamic viscosity for hydrogen is given in FIG 5. and FIG 6.

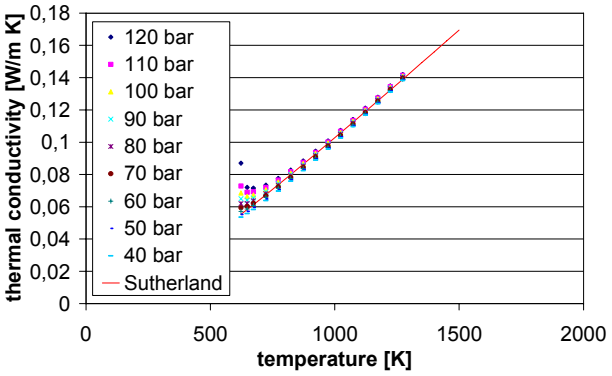

FIG 5. Temperature dependent thermal conductivity of steam and values from literature for various pressure levels.

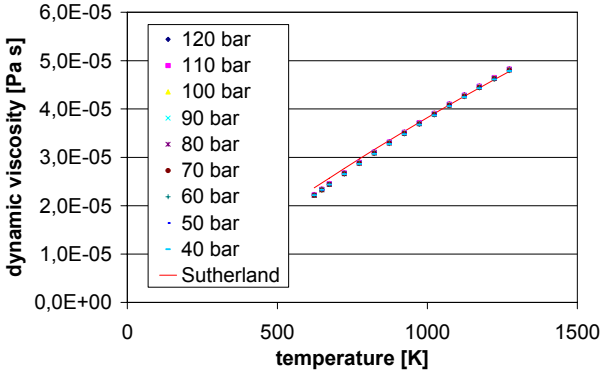

FIG 6. Temperature dependent dynamic viscosity of steam and values from literature for various pressure levels.

The good coincidence between the values from literature and the least square fitted Sutherland curves in FIG 5. and FIG 6. shows the suitability of the Sutherland equations to model the temperature dependency of the thermal conductivity and the dynamic viscosity of steam.

4.3. Determination of other material parameters

Due to restrictions of the available CFD program, values for the isobaric specific heat capacity and the isentropic exponent had to be used, which are constant and have identical values for both of the considered fluids. Average values for steam were taken for this purpose.

5. BOUNDARY CONDITIONS AND MESHING OF THE MODEL

5.1. Boundary conditions

The modeled area and its boundaries are shown in FIG 7.

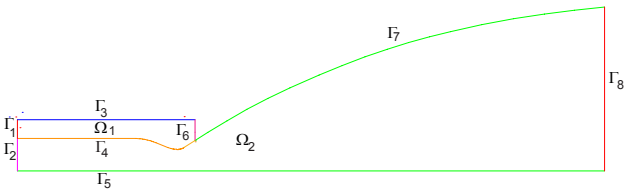

FIG 7. Modeled area and its boundaries.

The boundary conditions, which are assigned to the boundary lines shown in FIG 7, are given in TAB 1.

boundary description	remarks	boundary assignment	given values
hot gas input	As the combustion process is not included in the model, the hot gas is assumed to enter the combustion chamber at the injector plate with the hot gas pressure p_{hg} and the hot gas temperature T_{hg}.	Γ_2	$p_{hg} = 0.8MPa$ $T_{hg} = 3320K$
coolant input	The coolant is assumed to enter the porous combustion chamber wall material from a reservoir with the pressure p_{res} and the temperature T_{res}.	Γ_3	$p_{res} = 0.9MPa$ $T_{res} = 100K$
fluid output	At the exit plane, the mixture of the hot gas and the coolant leaves the nozzle extension. Because of the supersonic flow in the nozzle extension, no boundary condition is applied at the exit plane.	Γ_8	
surface of the nozzle extension	The nozzle extension is assumed to have no active cooling. Therefore, the tension velocity components normal and tangential to the wall are assumed to be zero.	Γ_7	$v_r = 0$ $v_x = 0$
symmetry line	On the rotatory symmetry axis, the thermal gradient and the velocity, both in radial direction, must be zero.	Γ_5	$v_r = 0$ $\frac{\partial T}{\partial r} = 0$
surface of the porous wall material	On the remaining boundaries of the porous combustion chamber wall material, the velocity in direction normal to the wall is set to zero.	Γ_1, Γ_6	$v_n = 0$

TAB 1. Assignment of the boundary conditions to the boundaries.

5.2. Meshing of the model

The mesh that is used for the CFD analysis is shown in FIG 8.

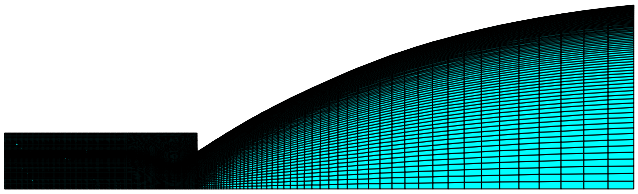

FIG 8. Meshing of the full model.

A zoomed version of this mesh is shown in FIG 9.

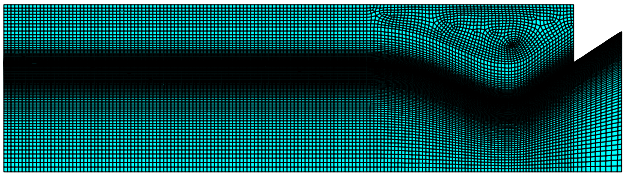

FIG 9. Meshing of the model in the area of the porous wall material.

The meshes in FIG 8. and FIG 9. show a

relatively coarse mesh on the axis of rotatory symmetry of the model (bottom line) as well as on the outside of the porous wall. However, in the vicinity of the interface between the chamber wall and the hot gas (boundary line Γ_4) as well as on the surface of the nozzle extension (boundary line Γ_7), a strong mesh refinement was performed.

6. ANALYSIS RESULTS

6.1. Pressure distribution

The pressure distribution in the combustion chamber is given in FIG 10.

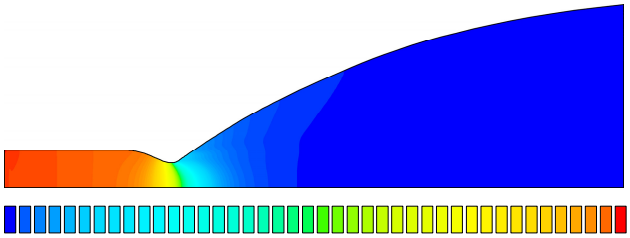

0.0009 MPa 0.45 MPa 0.9 MPa

FIG 10. Pressure distribution of the hot gas in the combustion chamber and the nozzle.

In the cylindrical part of the combustion chamber, the pressure is almost constant. However, in the vicinity of the nozzle throat, the pressure drops dramatically. The pressure distribution in the porous chamber wall is given in FIG 11.

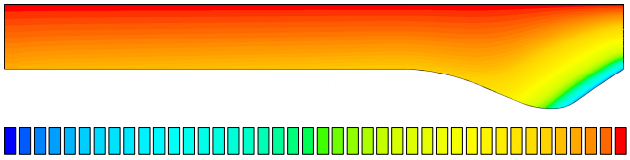

0.065 MPa 0.48 MPa 0.9 MPa

FIG 11: Pressure distribution of the coolant in the porous combustion chamber wall material.

In the cylindrical part of the chamber wall (left side of FIG 11), the pressure gradient is relatively small, points in radial direction and changes only slightly in axial direction of the combustion chamber. However, behind the nozzle throat (right end of FIG 11), the pressure gradient increases strongly.

6.2. Velocity distribution

The velocity distribution in the combustion chamber including nozzle is shown in FIG 12.

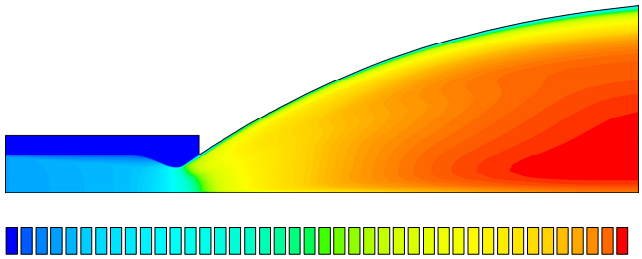

0 m/s 2251 m/s 4502 m/s

FIG 12. Velocity distribution of the hot gas and the coolant in a combustion chamber including the nozzle.

6.3. Temperature distribution

The temperature distribution in the combustion chamber including the nozzle is shown in FIG 13.

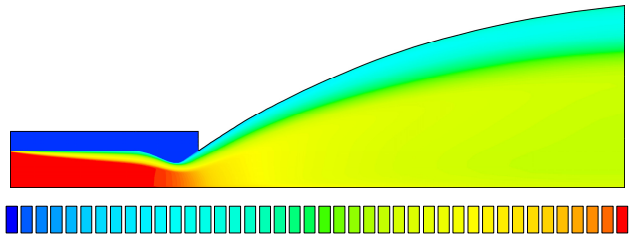

70 K 1695 K 3320 K

FIG 13. Temperature distribution of the hot gas and the coolant in a combustion chamber including the nozzle.

Unlike the pressure, which is almost constant in the cylindrical part of the combustion chamber, a temperature drop in radial direction can be observed in FIG 10, which increases in axial direction of the combustion chamber. This temperature drop is certainly caused by the coolant, which builds up an increasing film cooling on the surface of the chamber wall. This increasing film cooling can also be observed in FIG 14. in section 6.4.

6.4. Mass fraction distribution of the coolant

The mass fraction of the coolant in the combustion chamber including nozzle is shown in FIG 14.

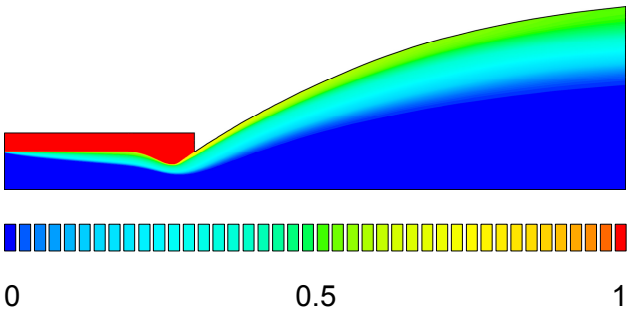

FIG 14. Mass fraction of the coolant in the hot gas and the chamber wall.

The film cooling effect of the coolant can be observed as a light blue (or light gray) layer of increasing thickness in FIG 14.

6.5. Specific mass flow rate of the coolant

The mass flow rate of the coolant at the surface of the combustion chamber wall is shown in FIG 15.

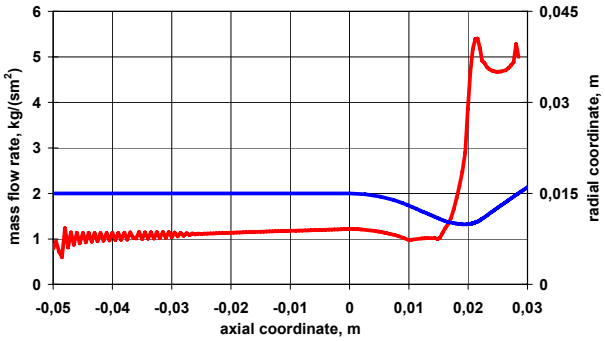

FIG 15. Specific mass flow rate of the coolant at the surface of the combustion chamber wall.

Due to the slightly increased dynamic pressure in the convergent part of the combustion chamber, the pressure difference between the hot gas and the coolant drops and therefore, the specific mass flow rate shows a local minimum in this part of the combustion chamber before it increases strongly behind the nozzle throat. This increase of the mass flow rate behind the nozzle (where a smaller mass flow rate would be sufficient because of the drop of the hot gas temperature) shows the necessity of an optimization of either the shape of the coolant input or the porosity of the combustion chamber wall.

6.6. Flow direction of the coolant

The flow direction of the coolant in the convergent part and the throat of the nozzle is shown in FIG 16.

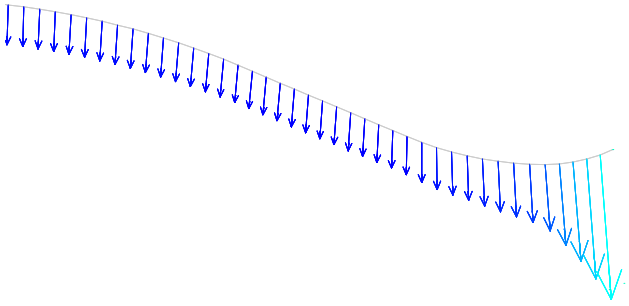

FIG 16. Flow direction of the coolant in the convergent part of the nozzle.

7. SUMMARY AND OUTLOOK

A methodology for a coupled CFD Analysis of the hot gas and the coolant flow in effusion cooled combustion chambers was presented. This methodology was successfully applied to model the flow field of a model combustion chamber. Further analyses at DLR Lampoldshausen will take into account a wider range of physical effects such as:

- hot gas and coolant specific values of the isobaric specific heat capacity and the isentropic exponent
- real gas effects of the hot gas and the coolant
- thermal conductivity of the porous combustion chamber wall material

8. REFERENCES

[1] D. Greuel, A. Herbertz, O.J. Haidn, M. Ortelt, H. Hald, “Transpiration Cooling Applied to C/C Liners of Cryogenic Liquid Rocket Engines”, AIAA JPC 2004 - 3682

[2] M. Ortelt, I. Fischer, S. Ghadiani, H. Hald, D. Greuel, O.J. Haidn, Empirical Verification of Effusion Cooled CMC Rocket Thrust Chambers, AIAA JPC 2005

[3] D.C.Wilcox, Turbulence Modeling for CFD, DCW Industries, 1998

[4] L. Davidson, An Introduction to Turbulence Models, Chalmers University of Technology, 1999

[5] S.B. Pope, Turbulent flows, Cambridge University Press, 2000